Large-Eddy Simulation of Flow Around Low-Pressure Turbine Blade with Incoming Wakes

V. Michelassi,* J. G. Wissink,† J. Fröhlich,‡ and W. Rodi§
Universität Karlsruhe, 76128 Karlsruhe, Germany

The flow around a low-pressure turbine rotor blade with periodically incoming wakes at a realistic Reynolds number is computed by means of large-eddy simulation (LES). The computed results are discussed in terms of phase-averaged and mean quantities. A comparison is made with an existing direct numerical simulation (DNS) for the same geometry and operating conditions. Particular attention is devoted to flow structures associated with the incoming wakes and their effect on the boundary layers. The analysis of the flowfield reveals patterns similar to those encountered in DNS and in LES of flow in the same geometry at a lower Reynolds number. Noticeable differences occur in the suction-side boundary layer, which exhibits a complete transition to turbulence for the present case.

Nomenclature

b	=	two-dimensional anisotropy tensor, where $\overline{b_{ij}}$ is equal to $\overline{u_i u_j}/2\bar{k} - \frac{1}{3}\delta_{ij}$
C	=	chord
C_f	=	skin-friction coefficient, $\tau_{\text{wall}}/(\frac{1}{2}\rho U_1^2)$
C_p	=	time-averaged static pressure coefficient, $2(\overline{p} - \overline{p_1})/U_1^2$
D	=	velocity defect, $|\langle \boldsymbol{v} \rangle| - |\bar{\boldsymbol{v}}|$
d	=	diameter
f	=	reduced frequency $(1/T) \cdot C/U_2$
$\bar{f}$	=	time average of f
$\langle f \rangle$	=	phase average of f
H	=	shape factor, δ^*/θ
h	=	spanwise extent
k	=	turbulent kinetic energy
l	=	pitch
n	=	direction normal to the wall
P_k	=	production rate of turbulent kinetic energy
p	=	static pressure
Re	=	Reynolds number
S	=	symmetric part of velocity gradient tensor
T	=	nondimensional time period, $1/|u_b|$
t	=	time
U	=	velocity magnitude
$\boldsymbol{v}$	=	velocity vector
β	=	flow angle
γ	=	stagger angle
δ^*	=	displacement thickness
θ	=	momentum thickness
λ	=	eigenvalue
τ	=	shear stress
Φ	=	phase
Ω	=	antisymmetric part of velocity gradient tensor

Subscripts

ax	=	axial
b	=	bar
w	=	wake
1	=	inlet
2	=	outlet

I. Introduction

THE high complexity of turbomachinery flows, which are three-dimensional, unsteady, and often transitional, requires powerful computational tools and models. In recent years computational methods as well as turbulence modeling based on classical Reynolds averaging have been improved to allow the successful simulation of two-dimensional,[1] quasi-three-dimensional,[2] and three-dimensional[3] realistic flows in turbine and compressor stages. The target of most of the simulations was the aerodynamics of the stator-rotor interaction and the rotor boundary-layer-wake interference.[4] In a real turbine stage, the unsteadiness and the disturbances convected by wakes generated by the preceding blade row are of great importance because they heavily affect the blade aerodynamic performances. Hence, in view of practical engineering applications, models able to predict the boundary-layer state have been developed in the past[5]; applications range from very crude algebraic models to complex, and more accurate, models based on transport equations.[2,6] Still, most of these formulations do not ensure sufficient generality in the presence of impinging wakes. Direct numerical simulation (DNS)[7,8] and large-eddy simulation (LES)[9,10] are able to provide a much deeper insight in the wake–boundary-layer interaction mechanism as compared to two-dimensional unsteady Reynolds averaged Navier–Stokes simulations.

On the experimental side, the effect of incoming wakes on boundary layers was investigated both on flat plates[11] and in linear turbine cascades.[12–15] The two cases revealed considerable differences in boundary-layer development due to the pressure gradients encountered in the latter flows. Apparently, the strong acceleration in the first 40–50% of turbine blades suppresses most of the velocity fluctuations in the wake core so that the boundary layer often stays laminar or relaminarizes[7,8,16] shortly after the leading edge.

Although the DNS of a realistic turbine stage is far beyond the capabilities of modern supercomputers, recent results have shown that both DNS and LES[17,18] allow a detailed examination of the wake transport and the consequent impact on the blade boundary layers. These refined simulations revealed how the vorticity convected by incoming wakes affect the near-wall flow.[7,8,16] In particular DNS of the flow around turbine blades with incoming wakes was successfully carried out at $Re = 5.18 \times 10^4$ (Refs. 7 and 16) and 1.48×10^5 (Ref. 8).

The DNS calculations are extremely costly, and the question arises whether similar results cannot also be obtained by LES with

considerably lower computational effort. LES calculations of the low-Reynolds-number case ($Re = 5.81 \times 10^4$) are compared with the DNS in Ref. 16 and show overall good agreement. Unfortunately, however, this case, in which intermittent separation occurs on the suction side near the trailing edge, is not representative of realistic design conditions. The present paper reports on LES of the flow around a low-pressure turbine blade with incoming wakes at a higher, more realistic Reynolds number, and the case at $Re = 1.48 \times 10^5$ simulated by Wu and Durbin[8] by DNS was chosen. The results are compared with this DNS and are analyzed in detail, with particular focus on the interaction of the wakes with the boundary layers on both the pressure and suction sides.

II. Geometry and Operating Conditions

The geometry is that of the low-pressure aft-loaded turbine blade T106, assembled in a linear test rig,[14,15] which was selected by Wu and Durbin[8] for their DNS. Because the blade aspect ratio (h/C) is 1.76, with a blade chord C of 100 mm, the flow at midspan can be considered two dimensional, thereby allowing three-dimensional simulations to be performed under the assumption of a homogeneous flow in the spanwise direction. The blade stagger angle γ, the inlet angle β_1, and the outlet angle β_2, defined with respect to the axial direction as shown in Fig. 1 are 30.72, 37.7, and -63.2 deg, respectively. In the measurements, which were carried out at $Re = 5.18 \times 10^4$ and 2×10^5, the effect of an upstream row of blades was simulated by a moving bar wake generator with a bar diameter to pitch ratio of $d_b/C = 0.02$. Unfortunately, the bar-to-blade pitch ratio is not an integer number (0.4/0.525). To yield

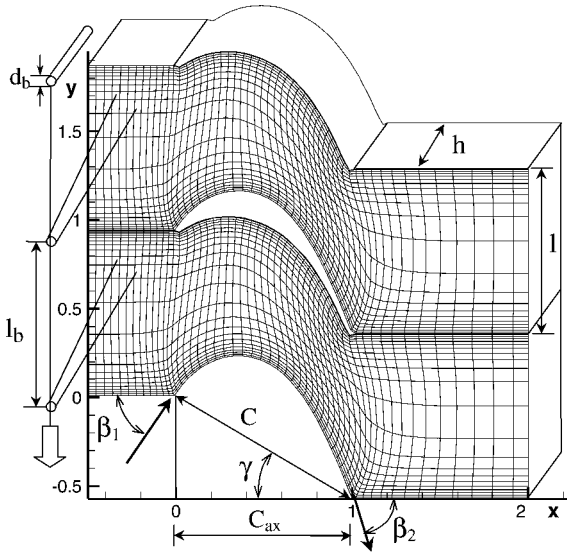an exactly periodic flow, the simulations should, hence, be carried out by using eight blade vanes, which would require an excessive number of grid nodes. Therefore, to reduce the computational effort and still have a reference data set, the operating conditions used in the DNS by Wu and Durbin[8] were selected. In this, l/C is 0.799, both the blade and wake pitch are 80 mm, and the Reynolds number, based on the axial chord and inlet conditions, is 1.48×10^5. If computed with the blade chord and exit conditions, as normally done in the turbomachinery field, the Reynolds number is 2.7×10^5.

III. Computational Details

A. Computational Grid and Flow Solver

The computational domain (Fig. 1) has been chosen to match the one employed in the DNS of Wu and Durbin,[8] which extends $0.5 \times C_{ax}$ upstream of the leading edge of the blades and $1.0 \times C_{ax}$ downstream of the trailing edge. The spanwise width is $h = 0.15 \times C_{ax}$. The grid was generated by the elliptic method proposed by Hsu and Lee,[19] which ensured a nearly orthogonal mesh close to the blade walls with $646 \times 256 \times 64$ nodes in the streamwise, pitchwise, and spanwise directions, respectively. In a previous DNS, Wu and Durbin[8] first tested a coarse grid, with $769 \times 257 \times 129$ points, and subsequently a refined one with $1153 \times 385 \times 129$ points. The refined DNS grid places 35–40 points inside the suction side boundary layer close to the trailing edge,[8] whereas in the present LES this number goes down to 15–20. This reduction was necessary to control the computational effort and, at the same time, to ensure a fair resolution of the incoming wakes vortical structures. Figure 2 shows the grid resolution on the suction side, which is the most demanding; the cell sizes in wall units in the x and z direction, Δx^+ and Δz^+, are below 70 and 15–20, respectively. Figure 2a, the plot of Δy^+, which is the distance of the cell center of the wall-adjacent cell to the wall in wall units, shows values around 3 for $x/C_{ax} < 0.55$ and goes down to 1 approaching the trailing edge, where the boundary layer thickens. These values indicate that the boundary layer is probably not sufficiently resolved for $x/C_{ax} < 0.6$–0.7. Along most of the pressure side, Δy^+ remains below 1.0. Only near the leading edge it reaches a peak of 2.0, and for $x/C_{ax} > 0.8$, it gradually grows until it reaches a value of 5.5 just upstream of the trailing edge.

The simulations have been carried out using the LESOCC[20] code, which discretizes the equations for incompressible flow by means of a second-order cell-centered finite volume method with centered interpolation of the fluxes. To avoid a decoupling of the velocity field and the pressure field, the momentum interpolation procedure of Rhie and Chow is employed.[21] The implicit solution of the Poisson equation for the pressure correction equation required by the employed SIMPLE method, originally adopted in Ref. 20, is complemented with a Fourier solver in the spanwise direction,[9] which substantially reduces the computational effort to enforce mass conservation. The equations are solved by marching in time with a three-stage Runge–Kutta algorithm. The mass conservation step was converged to a residual of 10^{-8}. The subgrid-scale (SGS) model

Fig. 1 Cascade geometry and grid used for LES (one out of 12 nodes is shown in both streamwise and pitchwise directions).

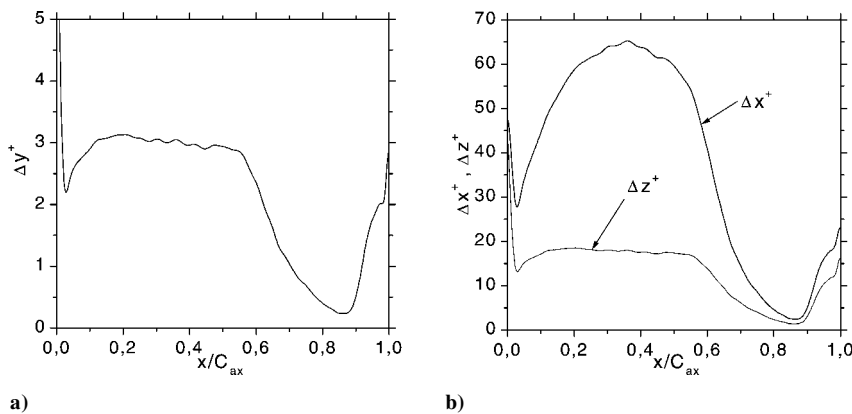a)   b)

Fig. 2 Distance between points in wall units at the blade suction side: a) distance of wall-adjacent point to the surface and b) wall-parallel point-to-point distances.

used in the LES is the dynamic model by Germano et al.[22] with the modification by Lilly.[23] It employs an eddy viscosity model together with a procedure of reducing the model constant whenever the flow is well resolved. For the present computation, the SGS model employs filtering and averaging in the homogeneous spanwise direction.

B. Boundary Conditions, Phase Averaging, and Computational Time

A no-slip boundary condition is enforced at the surface of the blade. The periodicity condition, enforced in the pitchwise direction, is not critical because the size of the expected flow structures is a small percentage of the blade pitch. In the spanwise direction as well, it is common practice to enforce the periodicity of the instantaneous flow because the dynamically relevant motions have a spanwise extent smaller than the size of the computational domain. The inflow boundary condition for the wakes is enforced by using the database that was kindly made available by Wu et al.,[17] who generated the incoming wakes with preliminary LES. In the current simulations the wake data closely resembles those adopted in the DNS.[8] The wake half-width is $0.04 \times C_{ax}$ combined with a maximum mean wake velocity deficit of 18%. The nondimensional tangential velocity of the wake is $u_b = -1.204$, and the time period, that is, one blade-pitch sweep of the wake, is $T = 0.77239$. (Throughout the paper, the inlet velocity U_1 and the axial chord C_{ax} are used as reference quantities.) To resolve the wake properly in both space and time, one period T is resolved with 10,240 time steps, which corresponds to a nondimensional time step of $\Delta t = 7.543 \times 10^{-5}$. When this value is adopted, the Courant–Friedrichs–Lewy number is always below unity. Phase averaging is performed every 160 time steps to obtain 64 equally spaced phase-averaged snapshots of the flowfield, labeled by their phase, $\Phi = 0/64–63/64$, whereas t/T is used for instantaneous quantities. Vectors are denoted in bold face. Like in the DNS, the phase-averaging process is initiated after five periods and subsequently performed over 10 periods. All computations were carried out by using 64 processors on the Hitachi SR-8000 vector-parallel computer of the University of Stuttgart with a total computational time of approximately 800 h.

IV. Time-Averaged Pressure Distribution Around the Blade

Figure 3 shows a comparison of the time-averaged static pressure coefficient $\bar{C}_p$ around the blade surface with the coarse and refined grid simulations of Wu and Durbin.[8] The flow encounters a strong favourable pressure gradient in the first 60% of the suction side, downstream of which the flow decelerates. On the pressure side, the pressure gradient remains substantially flat and close to zero in the first 50% of the blade. Farther downstream, the flow experiences a strong acceleration, which persists up to the trailing edge. Such behaviour is typical for mildly loaded low-speed turbine rotors. Figure 3 also shows that the static pressure coefficient predicted by the LES is in very good agreement with DNS on the entire pressure side as well as on the suction side up to 80% of the axial chord. For $x/C_{ax} > 0.8$, DNS and LES show some differences. Apparently the

pressure level predicted by LES is lower than that of DNS; the next sections will prove that this is linked to the boundary-layer state. Nevertheless, it is interesting to observe that the refined DNS plot deviates from the coarse DNS into the direction of the LES profile. In general, slight differences are located in the region where the flow experiences an adverse pressure gradient (APG), and a thickening of the boundary layer is expected.

V. Wake Migration and Dynamics

The wake is subject to severe straining inside the vane, as pointed out by Wu and Durbin[8] and, subsequently by Michelassi et al.[16] and Wissink[7] at a lower Reynolds number. The flowpath of the wake is linked to the principal axes of the time-averaged flowfield, which correspond to the eigenvectors of the strain-rate tensor and illustrate the direction of compression and stretching, as shown in Fig. 4a: the thin arrows identify the direction of stretching σ_1, and the thick ones identify the direction of compression σ_2. The magnitude of the vectors is not made proportional to the respective eigenvalues to ease the identification of the vector's direction. The direction and strength of the principal axes do not substantially change in time, as also suggested by Wu and Durbin[8] in their DNS of the same flow.

Figure 4b, in which the wake is traced by the velocity defect vectors $\langle v_w \rangle = \langle v \rangle - \bar{v}$, shows the impact of the background flow, in particular of the stretching and compression of the wake. When the wake is aligned with the direction of stretching as in the upper part of the vane, its width decreases as visualized by the two parallel
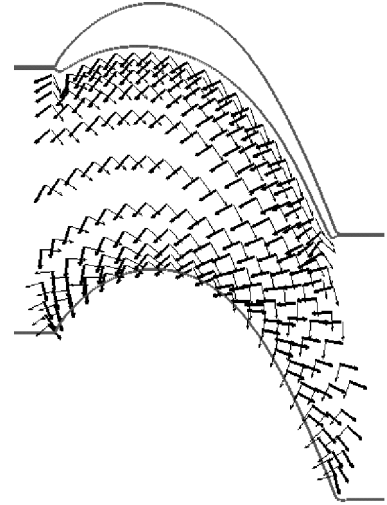

Fig. 4a   Principal axes of the time-averaged strain-rate tensor $\overline{S_{ij}}$, where thick vector identifies the direction of compression and the thin one that of stretching.

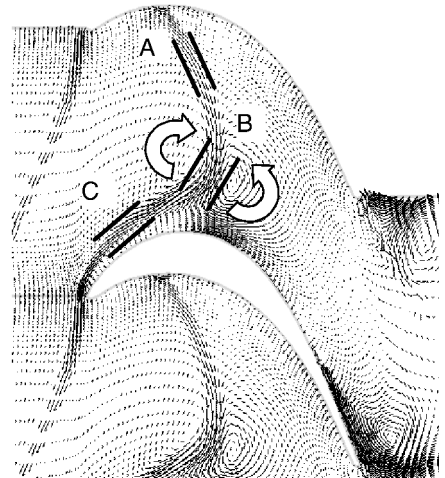**Fig. 3   Time-averaged static pressure distribution around the blade.**

Fig. 4b   Wake velocity $\langle v_w \rangle = \langle v \rangle - \bar{v}$ at $\Phi = 3/8$, where twin-thick parallel segments indicate the approximate width of the wake.
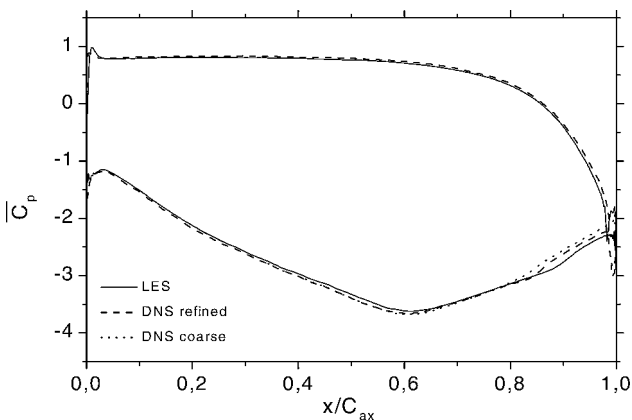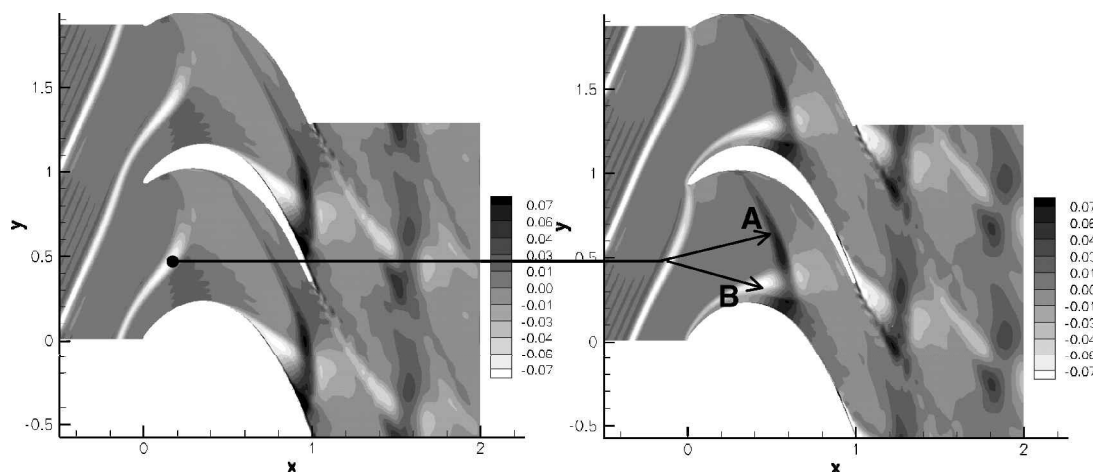
Fig. 5   Phase-averaged velocity defect D at $\phi = 0/8$ and $4/8$, from left to right.

lines labeled A in Fig. 4b. From the apex to the suction side, the wake is neither aligned with the direction of compression nor that of stretching so that its width remains almost unchanged with respect to the inlet. (See the parallel segments labeled C.) A totally different picture arises at the bow apex of the wake. Here the wake is almost perfectly aligned with the direction of compression so that it widens notably. (See the parallel segments labeled B.) Figure 4b shows the presence of two counter-rotating vortices around the wake which, together with the principal axis pattern, are in excellent qualitative agreement with what was discovered in the DNS.[8]

Figure 5 shows how the velocity defect D, defined as the difference between the magnitude of the phase-averaged velocity vector minus the magnitude of the velocity vector of the time-averaged field, can become positive. This phenomenon, already discovered in the DNS by Wu and Durbin,[8] can be explained as follows. Suppose the wake being straight and the vector $\langle \boldsymbol{v}_w \rangle$ vanishing remote from the wake. Then, $\langle \boldsymbol{v}_w \rangle$ has to be tangential to the wake because otherwise this contradicts continuity normal to the wake. If the wake is deformed, this remains qualitatively correct (the momentum exchange initiates $\langle \boldsymbol{v}_w \rangle$ in the surrounding fluid, small in the beginning and gradually increasing in time), which is visible in Fig. 4b. The vector $\langle \boldsymbol{v}_w \rangle$ changes its orientation to remain aligned with the position of the wake. This is clearly visible in Fig. 5. Hence, if $\langle \boldsymbol{v}_w \rangle$ has a component in the opposite direction of the mean flow, as it is the case upstream of the blades and in the lower part of the vane, this yields $D < 0$ as usual (see B at $\phi = 4/8$). If $\langle \boldsymbol{v}_w \rangle$ turns into the direction of the mean flow, as it happens in the upper part of the vane, this yields a positive velocity defect, $D > 0$ (see A at $\phi = 4/8$).

The three-dimensional visualization of the wake distortion requires identification of the incoming vortical structures. Jeong and Hussain[24] suggested to identify vortices by computing the second largest eigenvalue λ_2 of $S^2 + \Omega^2$. Wu and Durbin[8] found no differences when using either the instantaneous field or when first subtracting the spanwise mean velocity. Therefore, λ_2 was computed here using the instantaneous velocity field. Figure 6 shows isosurfaces of $\lambda_2 < 0$. The incoming vortical structures are clearly visible, and it is possible to follow their dynamics while the wakes travel across the blade vane. The snapshots refer to four instants equally spaced in time over one full period T. Before entering the turbine vane, only weak structures are visible, which are primarily oriented parallel to the wake. (See $t/T = 14$ in proximity to the leading edge of the upper blade.) The DNS[8] showed a more chaotic picture of the incoming vortical structures without any preferred orientation, probably because of the finer resolution of the grid in the flow core. As in the DNS,[8] the LES illustrates how the stretching aligns the vortices along the principal axis σ_1 near the pressure side. Along this direction, vorticity is amplified and, while the wake is gradually stretched, it evolves into elongated circular tubes that persist all along the pressure side of the blade. The local structures are
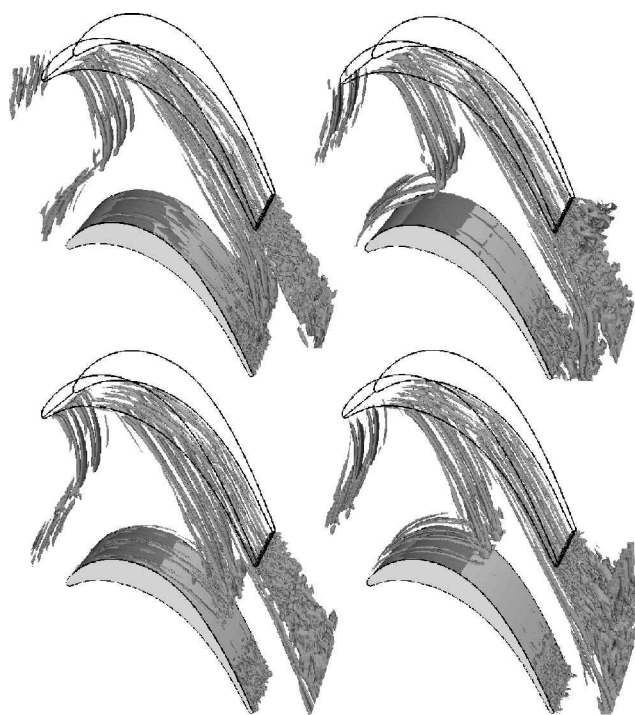

Fig. 6   Instantaneous isosurfaces of λ_2 in the blade vane for four selected times: $t/T = 14 + 0/8$, $14 + 2/8$, $14 + 4/8$, and $14 + 6/8$ from top left clockwise.

elongated, as illustrated by the increasingly large distance between the apex of the wake and the position of its impingement on the pressure side. Together with the progressive alignment of the wake with the direction of stretching, the vortex filaments become more and more distinct. Apparently LES allows capturing the essential features of the wake distortion as already evidenced by DNS: reorientation by convection ($t/T = 14$) and mean straining as the wake is swallowed into the turbine vane ($t/T = 14 + 2/8$), despite the reduced blade-to-blade grid resolution (165,000 nodes vs 440,000 of the DNS). Figure 6 also shows a difference between the lower and upper arms of the wake: The upper one shows regular and well-defined structures in proximity to the pressure side, whereas the lower one appears more chaotic and with a slightly superior degree of small-scale motion. In the DNS, this difference, located in the region of APG, was more pronounced. The discrepancy must be attributed to the reduction in the incoming wake resolution provided by the LES grid because it takes place sufficiently away from the suction side wall.
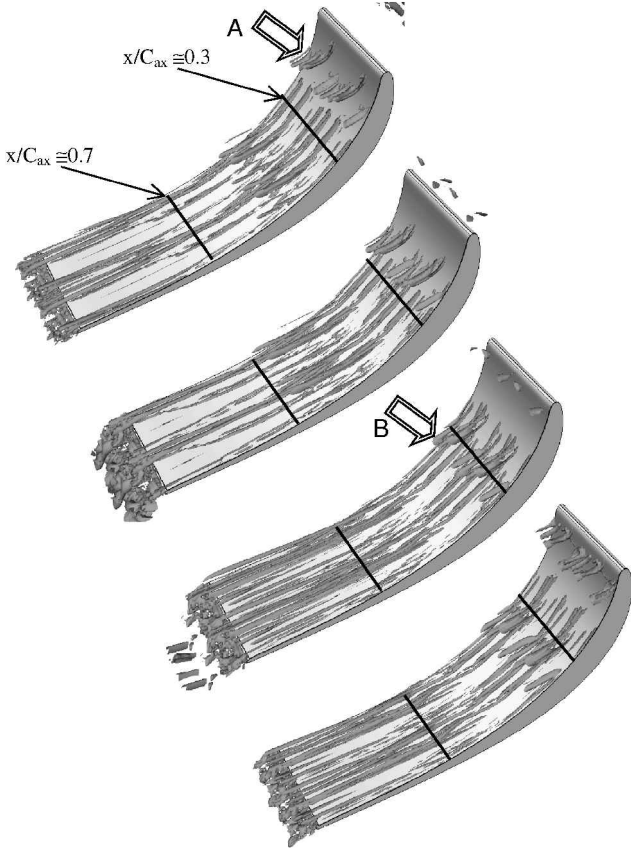
Fig. 7 Instantaneous isosurfaces of λ_2 in proximity to the pressure side for four selected times $t/T = 14 + 0/8$, $14 + 2/8$, $14 + 4/8$, and $14 + 6/8$ from top to bottom.

VI. Pressure Side

A. Flow Visualization and Flow Structures

In their DNS, Wu and Durbin[8] argued that the pressure side vortices are not Görtler vortices generated by the instability of the pressure-side boundary layer, but are flow structures stemming from the incoming vorticity of the wake. They corroborated their conjecture by plotting the λ_2 isosurfaces in proximity to the pressure side, similar to what is shown in Fig. 7 for the present LES. The elongated vortices correspond to those of Figs. 8 and 9 for two cross-flow sections close to the pressure side located at $x/C_{ax} = 0.3$ and 0.7, respectively. At $t/T = 14$, the incoming vorticity is evidenced by a small vortex core (arrow labeled A), which is convected and elongated downstream, while it progressively aligns with the pressure side.

In an attempt to verify the accuracy of the LES, this paragraph will repeat the same plots as given by Wu and Durbin[8] in their DNS of the same flow. Figure 8 shows the fluctuating velocity vectors, with the spanwise-averaged mean subtracted, in the plane located at $x/C_{ax} = 0.3$, as shown in Fig. 7, which extends 6% C_{ax} into the flow core from the pressure side. The eight consecutive instants, covering two time periods as in the DNS, show several counterrotating vortex pairs in the immediate proximity of the pressure side wall, for example, see $t/T = 15$ and 15.25.

Although a direct comparison of instantaneous flowfields is clearly impossible due to their random content witnessed by the differences between two consecutive periods, Fig. 8 shows flow patterns quite similar to the DNS. The large rotating structures visible at $t/T = 15.50$ and $0.05 < x < 0.10$, for example, belong to the wake, and they repeat at $t/T = 16.5$. These are qualitatively the same macrostructures identified in Fig. 7 by B at $t/T = 14 + 4/8$, the generation of which was discussed earlier: the longitudinal vortices turn into counter-rotating vortices near the wall, which causes up/downwash of low-/high-momentum fluid. The LES identifies weak and small vortices close to the wall, which have an oppo-

site sense of rotation with respect to those of the wake core due to the no-slip condition enforced at the wall already at $t/T = 15.50$. The vortical structures are in perfect agreement with the results given in Ref. 8. At $t/T = 15.75$, the cross section illustrates how the primary vortex disappears because it has gradually collapsed while approaching the wall, and it generates the two vortex pairs at $z = 0.075$ and 0.125. The two vortex pairs are gradually attenuated ($t/T = 16.00$ and 16.25) before the next wake crosses the plane at $x/C_{ax} = 0.3$, and the process is further iterated in time.

Figure 9 shows the crossflow plane located at $x/C_{ax} = 0.7$ at four instants. This plane is located farther downstream; hence, the wake arrives somewhat later. The negative fluctuating streamwise velocities produce a mushroomlike contour, as in the DNS, which corresponds to the transport of low-momentum fluid away from the wall promoted by each pair of counter-rotating vortices. This low-momentum fluid spreads in the spanwise direction and yields the structures shown in Fig. 9. As in the DNS, the mushrooms are often asymmetric, with the largest arm corresponding to the strongest of the two originating counter-rotating vortices. The comparison with the fluctuating velocity vectors of Fig. 9 for the same instants reveals a much more complex flow pattern than that encountered at $x/C_{ax} = 0.3$. This can be explained by looking again at the λ_2 isosurfaces of Fig. 7. At $x/C_{ax} = 0.3$, the pressure side experiences an intermittent growth and decay of the vortex structures. When proceeding farther downstream, the wakes, which are identified by the elongated vortices, are already virtually aligned with the blade wall and are found along the pressure surface for $x/C_{ax} > 0.3$–0.4 until the trailing edge. These structures are permanently present; again see Fig. 7. As a result, in this portion of the pressure side, the vortex filaments stemming from consecutive wakes overlap and generate a large number of structures. The final picture of the flow is remarkably more complex than that encountered for $x/C_{ax} = 0.3$, as shown by the fluctuating velocity plot of Fig. 9, and it substantially fits with the existing DNS.

B. Time- and Phase-Averaged Profiles

Figure 10 shows the status of the pressure-side boundary layer. For $x/C_{ax} > 0.1$, the skin-friction coefficient $\bar{C}_f$ grows due to the flow acceleration, which is mild in the first 60% of the blade and quite strong farther downstream. The values of $\bar{C}_f$ are always in the range of a laminar or early transitional boundary layer over a flat plate.[25] The boundary-layer edge, needed for the computation of boundary-layer integral parameters and $\bar{H}$, is determined by a procedure based on the local vorticity.[2] The shape factor experiences a sudden increase up to the value of 3 in proximity to the stagnation point, where the pressure gradient is first strongly adverse and then almost zero (Fig. 3). Farther downstream, up to $x/C_{ax} < 0.6$, $\bar{H}$ gradually reduces down to 1.8–2.0 due to the effect of the impinging wakes, and then it slightly rises again, leveling off at a value of 2.3 in the strongly favorable pressure gradient region. Apparently, the time-averaged boundary layer is never truly turbulent because $\bar{H}$ never drops below 1.8–2.0, despite the strong and intermittent disturbances discussed in the preceding section.

The time-averaged behavior of the flow on the pressure side may be better understood with the help of Fig. 11, which reports the phase-averaged shape factor $\langle H \rangle$ and the momentum thickness $\langle \theta \rangle$ for six sections normal to the pressure side wall located at 20, 40, 50, 60, 70, and 80% of the axial chord. The boundary layer has a strongly intermittent nature only in the first 60% of the axial chord, as proved by the up–down shape of the curves. Then, both the shape factor and the momentum thickness are nearly constant for $x/C_{ax} > 0.6$. Apparently, there is a mild increase of momentum transfer in the boundary layer due to the intermittent presence of the impinging wakes, causing some change of the velocity profile toward a turbulent boundary layer. Nevertheless, both the time-averaged and phase-averaged H values suggest that transition does not really take place. The three sections at $x/C_{ax} = 0.4$, 0.5, and 0.6 periodically become almost turbulent, $\langle H \rangle \cong 1.6$, but they relaminarize when the wake is far from the pressure side wall. The two sections farther downstream, $x/C_{ax} = 0.7$ and 0.8, show almost constant values for both quantities: the static pressure coefficient (Fig. 3) indicates
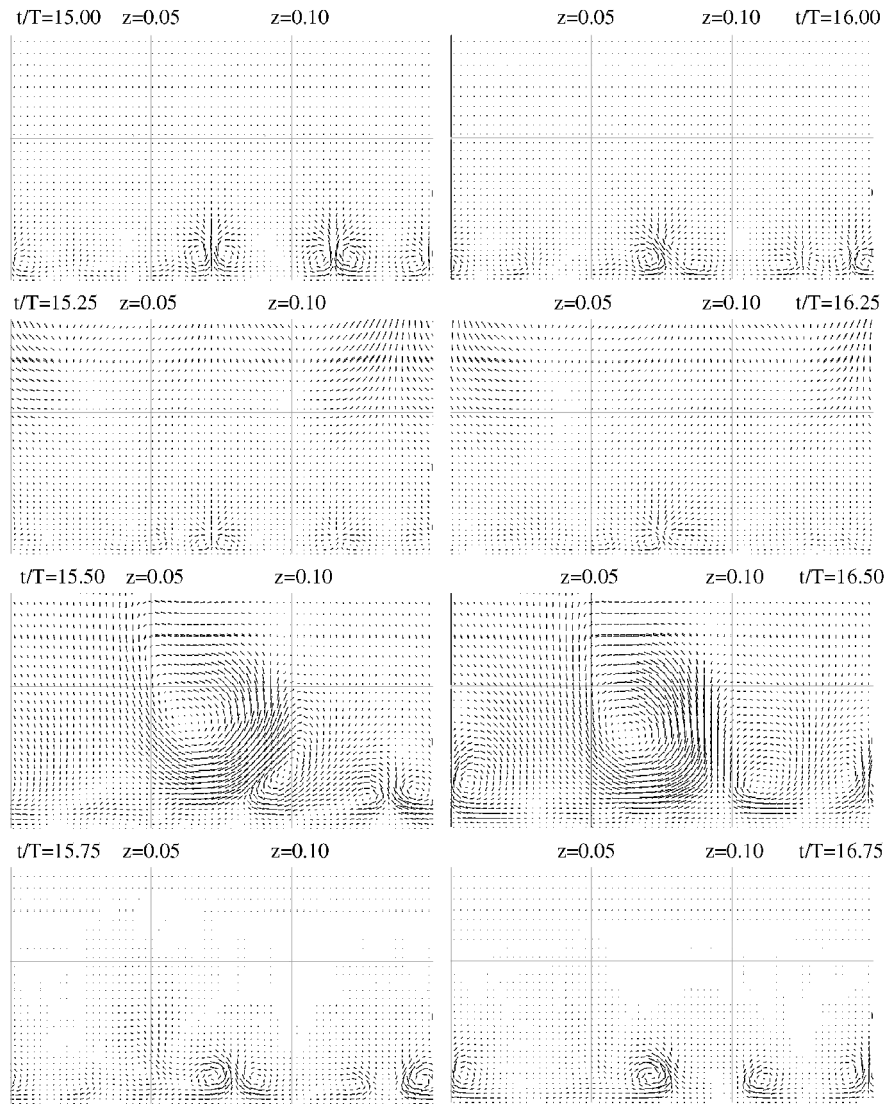
Fig. 8 Fluctuating velocity vectors (spanwise-averaged mean subtracted) in the plane perpendicular to the pressure surface, $x/C_{ax} = 0.3$, at eight consecutive instants $t/T = 15$–16.75, step $= 0.25$.

that the nearly constant-in-time nature of the boundary layer is due to the concerted action of the favorable pressure gradient and the overlap of several wakes for $x/C_{ax} > 0.6$, which masks the effect of each single incoming wake, as suggested by the λ_2 isoline plot of Fig. 7. At 60% of the axial chord, the shape factor reaches its lowest value: for this reason, both the phase-averaged turbulent kinetic energy and the production rate are shown at this section in Fig. 12. Close to the pressure side wall, for $n/C_{ax} < 0.02$ and for all phases, there is always a core with relatively large values of $\langle k \rangle$ and $\langle P_k \rangle$. Both are very moderately boosted by the impinging wakes (the position of which is shown by the black arrows for the first phase). The situation does not change in the other five cross sections, and the same happens when plotting the phase-averaged components of the Reynolds stress tensor.

To understand why the boundary layer remains substantially laminar despite the peak of k, Figs. 13, 14, and 15 show, respectively, the wall normal profiles of the time averaged velocity $\bar{u}$, the turbulent kinetic energy $\bar{k}$, and the normal stresses in the streamwise $\overline{uu}$ normal $\overline{vv}$ and spanwise $\overline{ww}$ directions at the same six axial locations, 20, 40, 50, 60, 70, and 80% C_{ax}, of Fig. 11. The DNS data[8] are also inserted for comparison. The time-averaged velocity profiles of Fig. 13 show that in the first two sections, 20 and 40% C_{ax}, the boundary layer is quite thick because of the nearly zero pressure gradient. It then narrows farther downstream due to the

strongly favorable pressure gradient encountered for $x/C_{ax} > 0.6$, the effect of which is visible in the $\overline{C_f}$ plot of Fig. 10. The good agreement with the profiles computed by Wu and Durbin[8] suggests that the velocity field predicted by the LES is fairly close to that given by the DNS.

Figure 14 shows a more challenging comparison by displaying profiles of the time-averaged turbulent kinetic energy at the same six sections. The profiles computed by the present LES report the resolved velocity fluctuations only without the SGS contribution. The turbulent kinetic energy peak as predicted by both DNS and LES constantly grows while proceeding toward the trailing edge. Still, if the turbulent kinetic energy peak is made nondimensional with respect to the local velocity, $\bar{k}/u_{loc}^2$, the ratio decreases, as shown in Fig. 16 with the exception of the first 40% of the blade. This suggests that the local turbulence intensity indeed decreases while approaching the trailing edge under the overwhelming effect of the favorable pressure gradient and that the boundary layer stays laminar. Except for the first section, the kinetic energy in the LES matches the DNS data fairly well. (In particular see the peak located at $n/C_{ax} \approx 0.004C_{ax}$.) The reasons for missing the shoulder at $0.01 < n/C_{ax} < 0.02$ are not totally clear, but probably stem from the reduced grid resolution in the flow core, where part of the contribution to k transported by the wake and resolved in the DNS is lost in the LES.
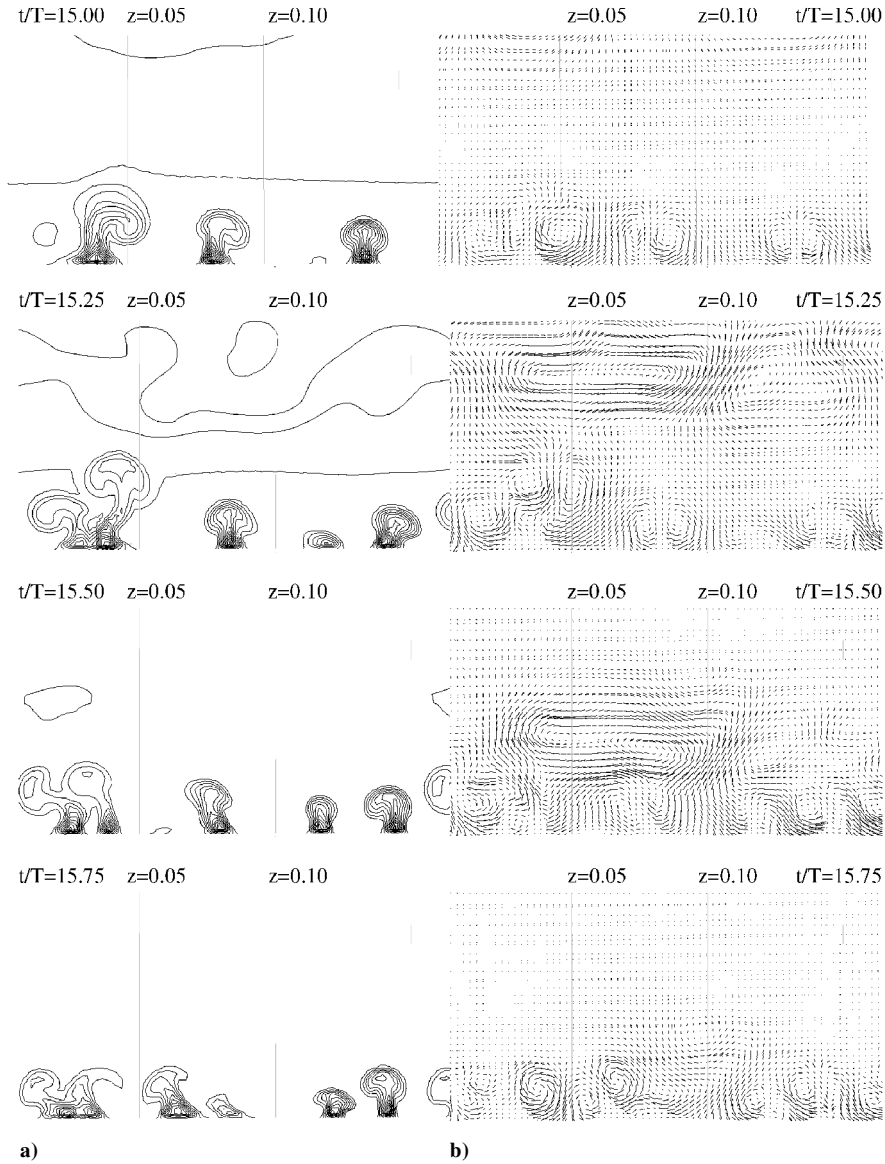
Fig. 9   Plane perpendicular to the pressure surface at $x/C_{ax} = 0.7$: a) negative fluctuating streamwise velocity component (with respect to spanwise-averaged mean) (contour level from 0 to -0.3, step -0.015) and b) fluctuating velocity vectors (spanwise-averaged mean subtracted).
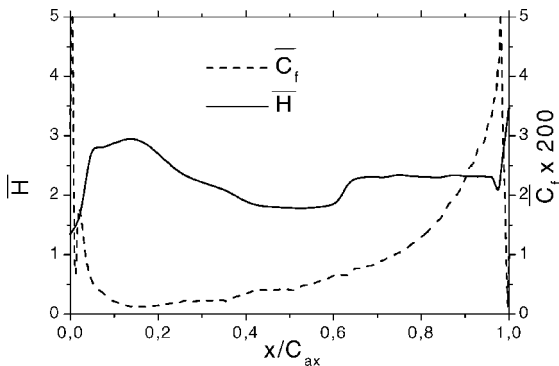

Fig. 10   Time-averaged $\overline{C_f}$ and $\bar{H}$ along the pressure side.

Figure 15 shows the three normal stresses and compares the spanwise component with the DNS. The various components are scaled differently to enhance visibility of the spanwise and normal stresses with respect to the streamwise component. The spanwise component compares favorably with the DNS, with the exception of the first section. The plots reveal that the streamwise component is approximately five times larger than the other two for each of the six sections, which is again in agreement with the DNS, reported

at one station, $x/C_{ax} = 0.30$. Hence, down to the trailing edge, the fluctuations are very anisotropic, and the overwhelming contribution to the peaks of $\langle k \rangle$ visible in Fig. 12 stem from the streamwise velocity fluctuations such that truly three-dimensional turbulence does not prevail. In fact, the fluctuations observed in the boundary layer correspond to the longitudinal vortices shown in Fig. 7, which are nothing else than the footprints of impinging wakes. Wu and Durbin[8] suggest that these vortices promote the up/downwash of low-/high-momentum in the boundary layer. The large difference in magnitude between streamwise fluctuations and normal and spanwise fluctuations, respectively, can be explained by the findings that the straining of plane wakes by the freestream velocity can promote unidirectional fluctuations to become an order of magnitude larger than fluctuations in other directions.[26] The lack of fully three-dimensional turbulent activity is also confirmed by the relatively weak correlation between u and v fluctuations as witnessed by the structural parameter $\overline{uv}/k$. At $x/C_{ax} = 0.6$, where the time-averaged shape factor is minimum, this ratio has always values about half the size of those observed in a fully turbulent boundary layer, that is, at $y^+ \approx 10$–12, a value of 0.058 is obtained instead of 0.10–0.12. This is the reason why the boundary layer never develops full turbulence, despite some sudden drop of the shape factor at around $x/C_{ax} = 0.6$. Farther downstream, the relative magnitude of the various components does not change because the strong favorable pressure
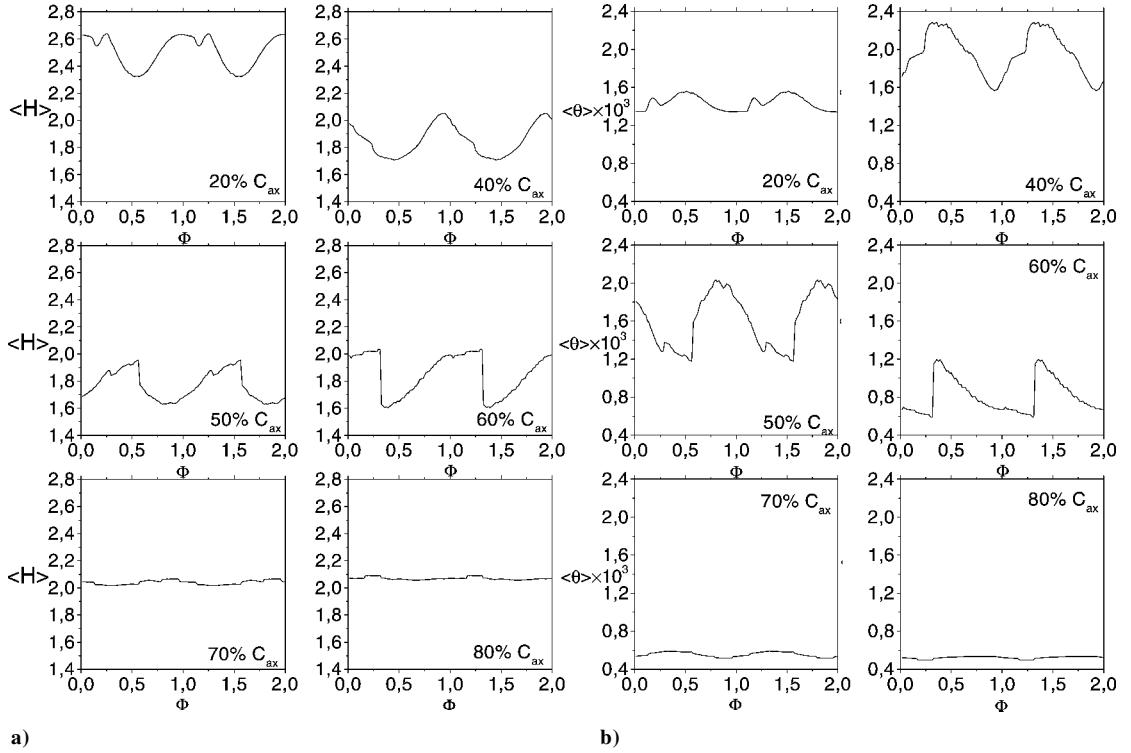
Fig. 11   Six sections at 20, 40, 50, 60, 70, and 80% C_{ax}: a) phase-averaged shape factor and b) momentum thickness.
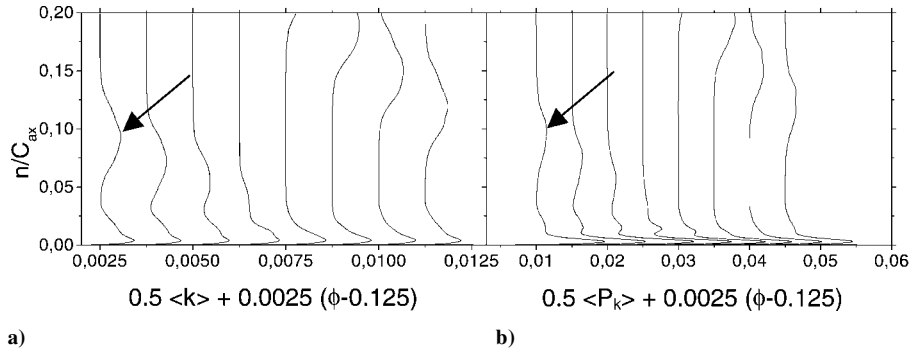

Fig. 12   Phase-averaged instants (eight curves for $\phi = 0$–0.875, step 0.125 from left to right): a) turbulent kinetic energy and b) production rate at 60% C_{ax}.

gradient inhibits the growth of the disturbances introduced by the wakes.

VII.   Suction Side

In this section we discuss the transition scenario on the suction side as described by the present LES and perform some comparison with the DNS of Wu and Durbin[8] to investigate the impact of the LES modeling on transition. The DNS reveals a relatively complex scenario. The presence of the impinging wakes causes transition near the leading edge. Past transition, there is a region that remains turbulent at all times due to the strong APG, visible in Fig. 3, and the way the wakes wrap around the nose of the blade. Because of the favorable pressure gradient farther downstream, the flow subsequently relaminarizes. Beyond $x/C_{\mathrm{ax}} \approx 0.6$, the boundary layer again experiences an APG, inducing deceleration. In the presence of impinging wakes, Wu and Durbin found evidence of bypass transition with turbulent spots appearing near midchord, which grow and merge into the fully turbulent trailing-edge region. The differences between this bypass transition scenario and the case without wakes are discussed in Ref. 8. In Fig. 17, the skin friction $\overline{C_f}$ along the suction side obtained with the LES is compared with the DNS result. The decrease of $\overline{C_f}$, starting just upstream of $x/C_{\mathrm{ax}} \approx 0.6$,

corresponds to the pressure gradient changing from favorable to adverse (Fig. 3). For $x/C_{\mathrm{ax}} < 0.75$, both curves are in good agreement. Downstream of this point, however, the DNS curve starts to increase at $x/C_{\mathrm{ax}} = 0.78$, whereas for the LES this takes place later, at $x/C_{\mathrm{ax}} = 0.87$. Because this increase is directly related to the transition of the boundary layer, we conclude that in the LES transition is delayed by about $0.1 C_{\mathrm{ax}}$ compared to the DNS.

To assess the behavior of the present LES, isoline-plots of the v velocity component were generated, which are equivalent to Fig. 8 in Ref. 8. They are reported in Fig. 18 for instants corresponding to the four different phases considered here. The backplane serves to identify the instantaneous position of the wake. As expected from an LES, the fluctuations in the v velocity contours are smaller than those obtained in the DNS. Near the leading edge, the effect of the wakes is much smaller. Between $t/T = 15.50$ and 15.75, for instance, the wake introduces small disturbances, but these are not able to trigger real turbulence. Instead, their lifetime is so short that one-quarter of a period later, they are almost completely damped out. A proper description of the leading-edge transition by LES is thought not to be important because the favorable pressure gradient farther downstream will damp out the generated fluctuations anyway. Downstream of $x/C_{\mathrm{ax}} = 0.6$, the pressure gradient becomes adverse again. Although in the area where the pressure gradient is favorable
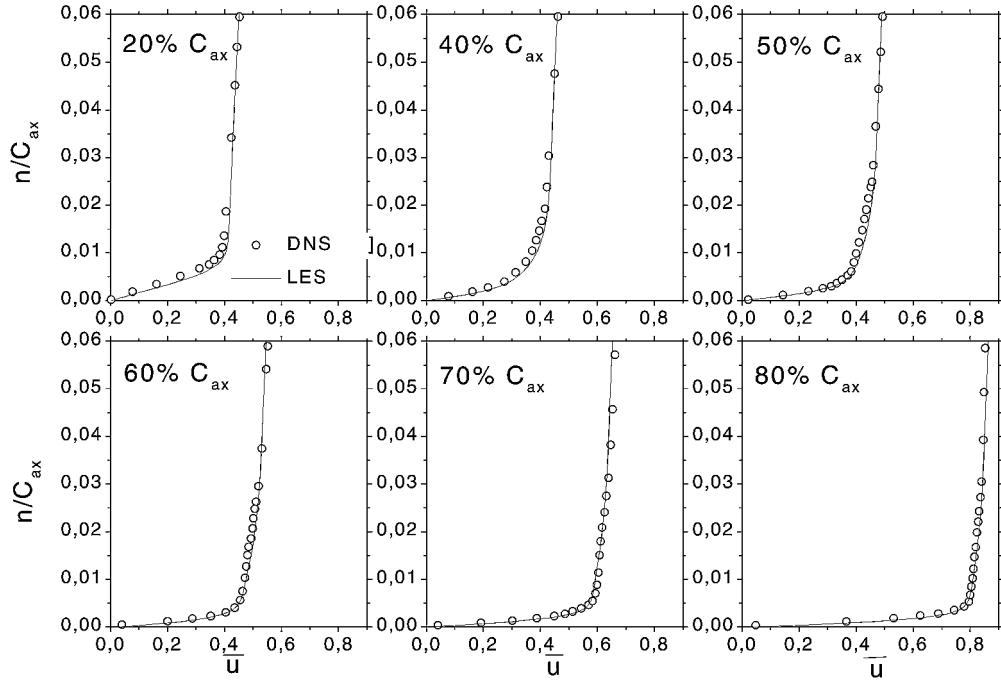
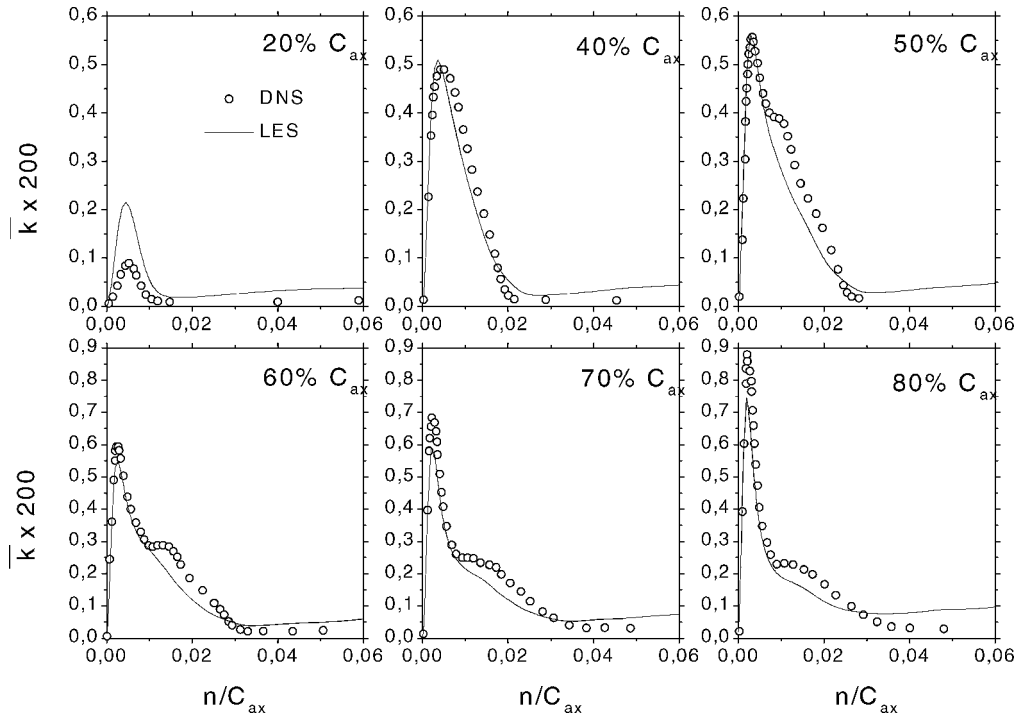Fig. 13   Profiles of time-averaged velocity at 20, 40, 50, 60, 70, and 80% C_{ax}: ——, present LES and ○, DNS.

Fig. 14   Profiles of time-averaged turbulent kinetic energy at 20, 40, 50, 60, 70, and 80% C_{ax}: ——, present LES and ○, DNS.[8]

the impinging wake hardly affects the v velocity inside the boundary layer, downstream of $x/C_{ax} = 0.6$ the effect of the impinging disturbances on the v velocity is clearly visible (Fig. 18 at $t/T = 15.00$). Hence, contrary to the skin-friction plot suggesting that there are no major differences between LES and DNS for $x/C_{ax} < 0.8$, the v velocity contours tell a different story. The perturbations observed in the region $0.6 < x/C_{ax} < 0.8$ are far too smooth to correspond to turbulent spots. Because the results of Ref. 8 show that the turbulent spots are triggered by the impinging wakes, two different causes may be responsible for their suppression in the LES. It is possible that the resolution of the suction-side boundary layer in the LES

is too coarse to represent sufficient fine-scale fluctuations, resulting in the damping of otherwise unstable modes by eddy viscosity. Furthermore, the wake might be damped excessively on its way from the inlet until it impinges onto the blade. This could be a consequence of the relatively coarse mesh used in the core region. (A similar phenomenon is observed on the pressure side, where the knee in the $\bar{k}$ profiles of Fig. 14 is lost due to the grid resolution of the impinging wakes.) Values of the eddy viscosity inside the wakes reach up to five times the molecular viscosity, thereby damping the small-scale wake fluctuations. The trailing-edge region is fully turbulent in both DNS and LES. In the LES, however, this region is
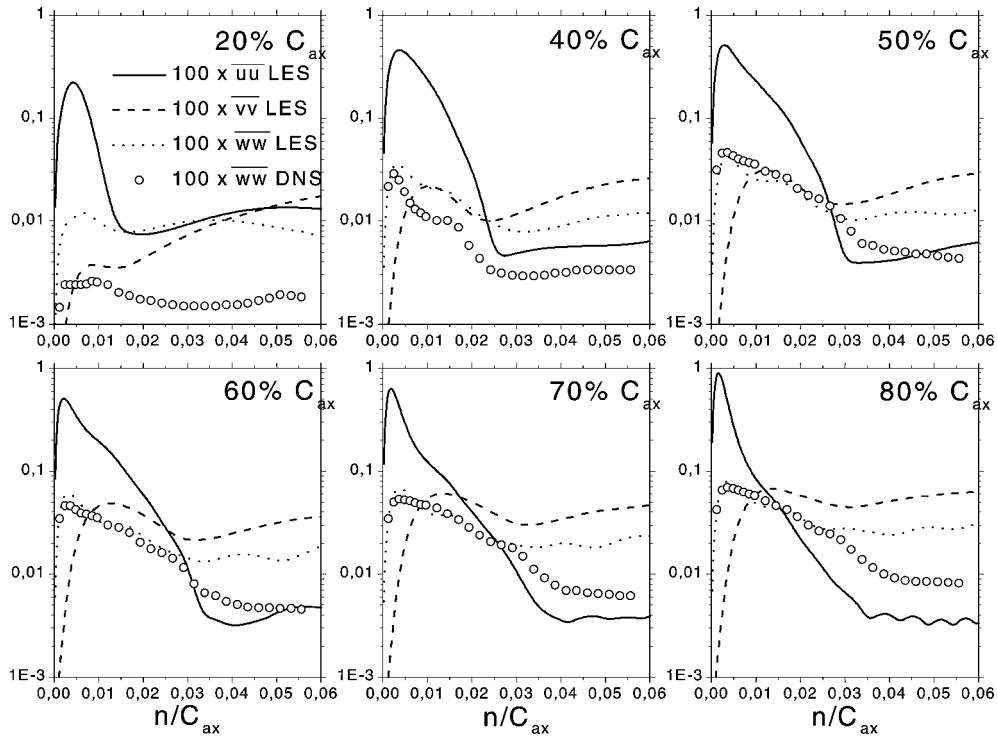
Fig. 15   Profiles of normal stress components in the streamwise direction ($\overline{uu}$), in the blade-normal direction ($\overline{vv}$), and in the spanwise direction ($\overline{ww}$) at 20, 40, 50, 60, 70, and 80% C_{ax}: ——, –––, and . . . ., present LES data; and ○ , DNS data.[8]
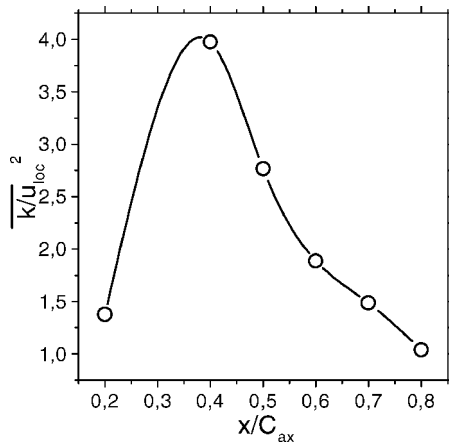

Fig. 16   Turbulent kinetic energy peak made nondimensional with respect to the peak velocity u_{loc}, close to the pressure side wall.
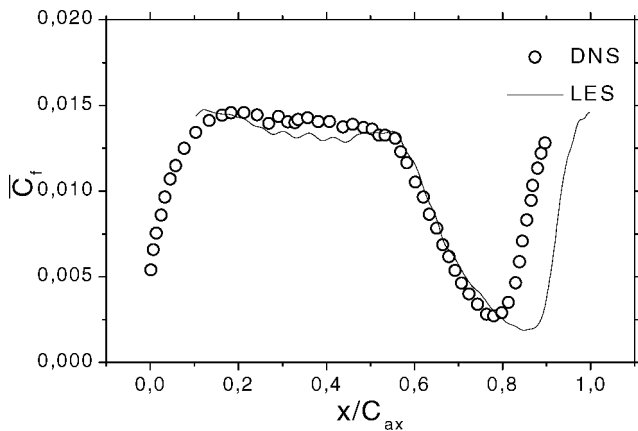

Fig. 17   Time-averaged $\overline{C_f}$ (×10) over the blade suction side; DNS results are given in Ref. 8.
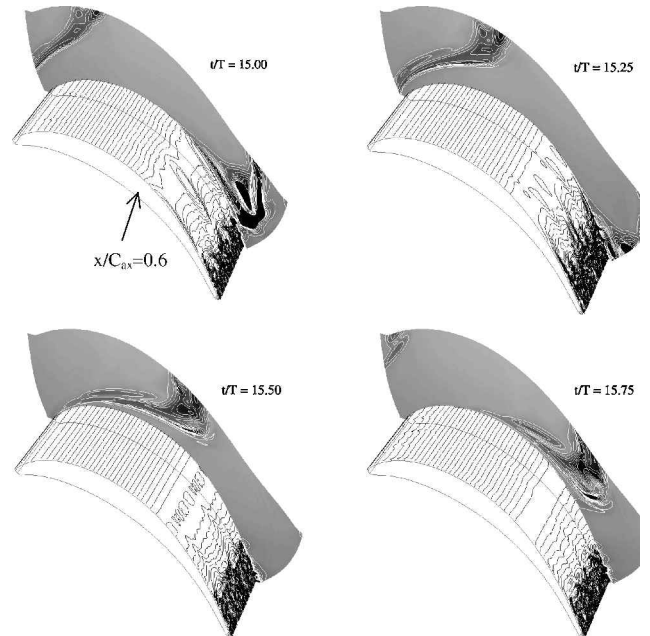

Fig. 18   Isolines of the v velocity component over the suction side surface, generated on grid plane $j = 4$ at about $0.002C_{ax}$ from the surface of the blade. Gray-scale on the backplane corresponds to the fluctuating velocity and is added to identify the location of wakes.

found to be smaller than in the DNS, due to the late transition in the LES already observed in Fig. 17.

Phase-averaged data are presented next. Figure 19 shows wall-normal profiles of the tangential velocity, the spanwise fluctuations $\langle w'w' \rangle$, and the fluctuating kinetic energy $\langle k \rangle$ at $x/C_{ax} = 0.8$ and 0.9. Before transition, the difference between the velocity profiles at various phases is almost negligible, reflecting a relatively small influence of the wakes on this quantity. In Fig. 19, it is shown that, compared to the fluctuating kinetic energy, at $x/C_{ax} = 0.8$ the spanwise
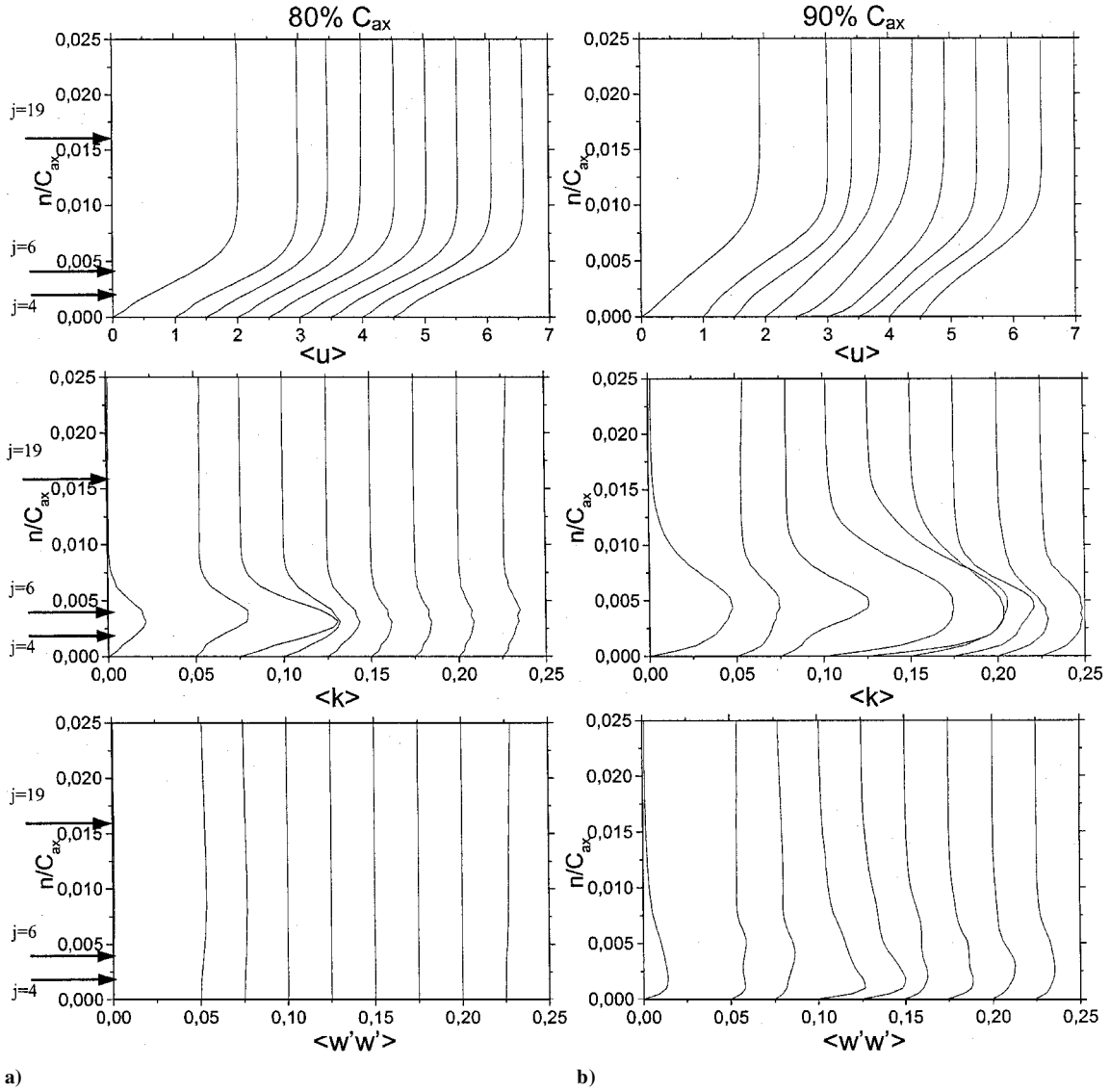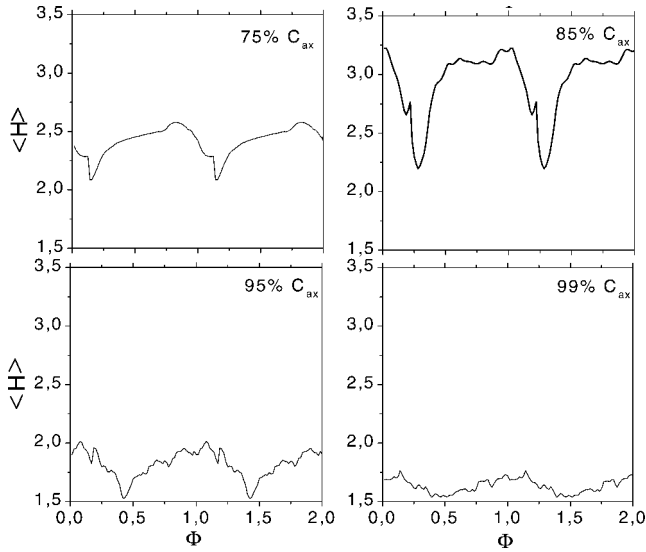
Fig. 19 Profiles normal to the suction side of the blade of tangential velocity, fluctuating kinetic energy $\langle k \rangle$, and spanwise turbulent stress $\langle w'w' \rangle$; eight phase-averaged fields at $\Phi = 0/8–7/8$; the leftmost profile is the time-averaged one: a) $x/C_{ax} = 0.8$ and b) $x/C_{ax} = 0.9$.

fluctuations are negligibly small for all phases. Hence, the fluctuating kinetic energy results almost entirely from two-dimensional fluctuations. At $x/C_{ax} = 0.9$, the situation has changed in that three-dimensional fluctuations are now present, particularly close to the wall. The fluctuating kinetic energy as well as the shear stress (of similar shape as $\langle k \rangle$, but not shown) have their maxima at a larger distance from the wall than before. Also the velocity profiles exhibit more variation from one phase to the other in response to the wakes. The profiles of the spanwise turbulent fluctuations $\langle w'w' \rangle$ plotted in Fig. 19 show that in the LES the fluctuations in the suction-side boundary layer change over from two dimensional to three dimensional in the range $0.8 < x/C_{ax} < 0.9$. At $\phi = 2/8$, a peak in the spanwise fluctuations is obtained very close to the wall at $x/C_{ax} = 0.9$. According to Fig. 18 ($t/T = 15.25$), at this phase the wake impinges somewhat upstream of the trailing edge. For larger ϕ, Fig. 19 for $x/C_{ax} = 0.9$ shows a gradual spreading of the spanwise fluctuations away from the wall. At the same time, the spanwise fluctuations close to the wall become smaller. That at $\phi = 2/8$ the impingement of the wake near $x/C_{ax} = 0.9$ coincides with a maximum in the spanwise fluctuations indicates that the production of turbulence near the wall is triggered by the wake.

As discussed ealier, the boundary layer remains virtually laminar despite the incoming wakes for roughly the first 80% of the blade axial chord. An analysis of what happens close to the trailing edge

reveals some interesting features. This analysis is performed with the aid of the phase-averaged shape factor $\langle H \rangle$, plotted in Fig. 20 for four sections at 75, 85, 95, and 99% of the blade axial chord. At $x/C_{ax} = 0.75$, the position of the wake is located directly to the right of the maximum of $\langle H \rangle$. Its effect on the shape factor is significant, although $\langle H \rangle$ never manages to drop below the value of 2. This suggests that the boundary layer remains basically laminar at all times. When moving farther downstream, at $x/C_{ax} = 0.85$, the effect of the wake is found to be amplified. This is due to the persistence of a moderate APG. At $x/C_{ax} = 95\%$, the shape factor is constantly below 2, indicating a definite presence of turbulence. Shortly after the wake has passed, $\langle H \rangle$ drops to 1.5, a value typical for turbulent boundary layers. Right at the trailing edge, at $x/C_{ax} = 0.99$, the transition is complete since the shape factor is constantly below 1.7.

We proceed analyzing the transition scenario using so-called x-Φ space–time plots of the phase-averaged fluctuating kinetic energy at various distances from the wall. The monitoring surfaces are identical with grid planes $j = 2, 6, 19$, and 62, as shown in Fig. 21, and follow the surface of the blade. They are located at the first grid node adjacent to the wall (surface 2), inside the boundary layer (surface 6), beyond but still close to the boundary layer (surface 19), and in the free-stream (surface 62). Figure 21 shows their nondimensional distances from the wall (computed by using the friction velocity

Fig. 20 Phase-averaged shape factor ($\langle H \rangle$) for four sections normal to the suction-side wall at $x/C_{ax} = 0.75, 0.85, 0.95,$ and 0.99.
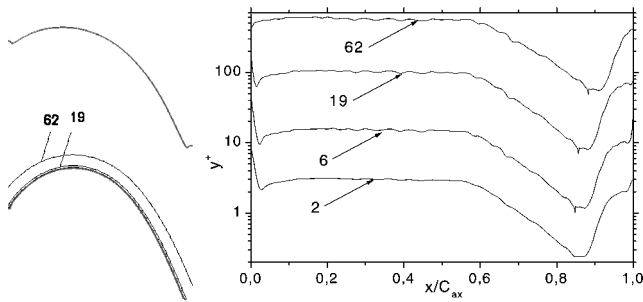
Fig. 21 Selected monitor surfaces and their distance from the suction side of the blade in wall units.

of the time-averaged flowfield). Their wall-normal distances (measured at the crown of the blade, $x = 0.35$) is $n/C_{ax} = 0.0008, 0.004, 0.016,$ and 0.073, respectively, which allows a relation to the plots in Fig. 19 to be drawn, where the corresponding levels are marked with arrows (except 2).

Along these monitoring surfaces, the phase-averaged fluctuating kinetic energy was computed using the 64 phase-averaged flowfields and is shown in Fig. 22. To improve visibility, the levels shown are not the same in all panels. The thick white line labeled w has been introduced as a reference line for comparison and corresponds to the position of the wake at the edge of the boundary layer. This position as a function of time has been determined assuming that the wake is passively convected by the freestream (as supported by the results of the DNS of Wu and Durbin[8]). For this, the inverse of the mean axial velocity at the edge of the suction-side boundary layer was integrated in the axial direction to determine the path of the wake in axial coordinates. The leftmost panel in Fig. 22 shows that on the surface 2, closest to the suction side boundary, there always exists a portion of flow that shows some turbulence activity, namely, from $x/C_{ax} \approx 0.85$ until the trailing edge. This corresponds with the transition discussed earlier, with respect to the time-averaged flow (Fig. 17). Note that the impinging wake only weakly triggers transition along this surface.

For surface 6, shown in the second panel, the influence of the impinging wake on the location of transition is much more pronounced. Each time the wake impinges, the location of transition moves upstream from $x/C_{ax} \approx 0.85$ to 0.65. The coincidence of the impinging wake with the onset of transition is illustrated by the solid black circle, which shows that the increase in the fluctuations is clearly aligned with the wake path. As already noted, Fig. 19 clearly shows that these fluctuations are effectively two dimensional; how-

ever, farther downstream, for $x/C_{ax} = 0.85$, spanwise fluctuations become more important. We can summarize that in the LES transition appears to take place via amplification of two-dimensional modes followed, farther downstream, by the amplification of three-dimensional modes, which are triggered by the impinging wakes (as observed in Fig. 19 for $x/C_{ax} = 0.9$). The periodic pattern of Fig. 22, second panel, suggests that the wake is responsible for the increase of the fluctuating kinetic energy starting shortly after $x/C_{ax} = 0.5$. From this point onward, this plot shows the same pattern as identified by Schulte and Hodson,[13] who measured the wake-induced transitional flow for a similar turbine blade, labeled blade H, in Ref. 13, with a pitch-to-chord ratio of 0.78 and $Re = 1.3 \times 10^5$ based on chord and exit conditions. (Observe that the Reynolds number based on the axial chord and inlet conditions is approximately 5.6×10^4 vs the value 1.48×10^5 of the present simulation.) They suggest the presence of a turbulent region clearly triggered by the incoming wakes. In our LES, we obtain a region of transitional flow in the triangular-shaped portion of the suction-side boundary layer labeled a (Fig. 22, surface 6). Once the effect of the wake is damped out, the measurements suggested the presence of a so-called "becalmed" region in which turbulence is substantially absent. This coincides with the dark region, labeled b in Fig. 22, that separates the two lighter regions. Note that the becalmed region survives until the next wake passes, but it never reaches the trailing edge of the blade where the boundary layer remains turbulent all of the time. Surface 19 is located near the edge of the boundary layer. Therefore, the mean axial velocity at this surface is comparable to the mean axial velocity at the edge of the boundary layer; for this reason, the path of the wake coincides with the axis of the "tongue" of fluctuating kinetic energy starting at $x/C_{ax} \approx 0.15$ and $\phi \approx 0.55$. This illustrates that it is possible to use the fluctuating kinetic energy to identify the path of the wake. Note that the level of $\langle k \rangle$ is an order of magnitude lower at this distance, though (also Fig. 19). Surface 62 is located in the freestream. Here, the levels of fluctuating kinetic energy reached inside the wake are much higher than the levels observed at surface 19. This is a direct consequence of the kinetic energy production inside the bow apex of the wake inside the freestream and core region of the flow. The detailed study of this mechanism is the subject of a companion paper (Michelassi, V., and Wissink, J., "Turbulent Kinetic Energy Production in the Vane of a Low-Pressure Linear Turbine Cascade with Incoming Wakes," to be submitted for publication). Like for surface 19, again the fluctuating kinetic energy identifies the path of the wake as it crosses the surface, which for surface 62 clearly differs from the path of the wake as it impinges on the edge of the boundary layer. This phase lag results from the U shape of the wake shown in Fig. 6 and the backplanes in Fig. 18 (Ref. 8). The wake advances faster in the core of the flow and is slower at the blade. Hence, the wake at surface 62 is ahead of the white line w because the latter is related to the position of the wake closer to the surface. On the contrary, the wake lags behind this line for surfaces 2 and 6 in the leftmost two panels of Fig. 22.

An important result of the plots in Fig. 22 is that the wakes do not interact with one another. Hence, the results can be compared to cases with wakes having a different, in particular lower, frequency. The reason for this weak interaction probably also stems from the relatively small wake strength (half-width $= 0.04 \times C$, with maximum wake velocity deficit $= 18\%$), which is directly proportional to the disturbance convected downstream. An often employed quantity to characterize the wake–wake interaction is the so-called reduced frequency f, which compares the incoming wake period with the approximate time the wake takes to travel inside the vane, C/U_2. Whereas in the measurements of blade H (Ref. 13) the reduced frequency is $f = 0.38 - 0.78$, it is $f = 1.08$ in the present investigation, which is only marginally larger. Figure 22 shows that also for this reduced frequency the wakes are far enough apart to avoid wake–wake interaction inside the turbine cascade passage. This means that the results presented here can be compared to other experiments or numerical simulations, having similar geometry and Reynolds number, which also exhibit negligible wake–wake interaction.
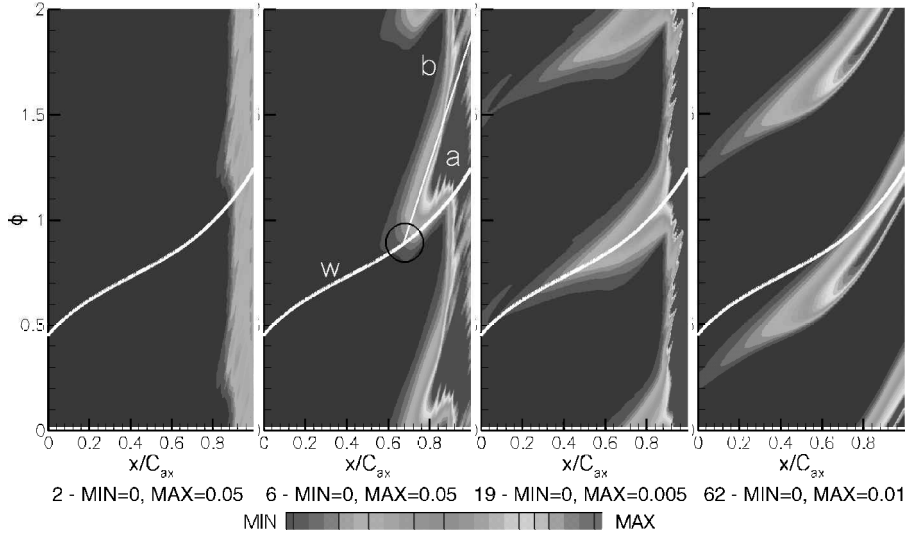
Fig. 22   Space–time plots of the fluctuating kinetic energy along selected surfaces (*x* axis aligned with axial chord).
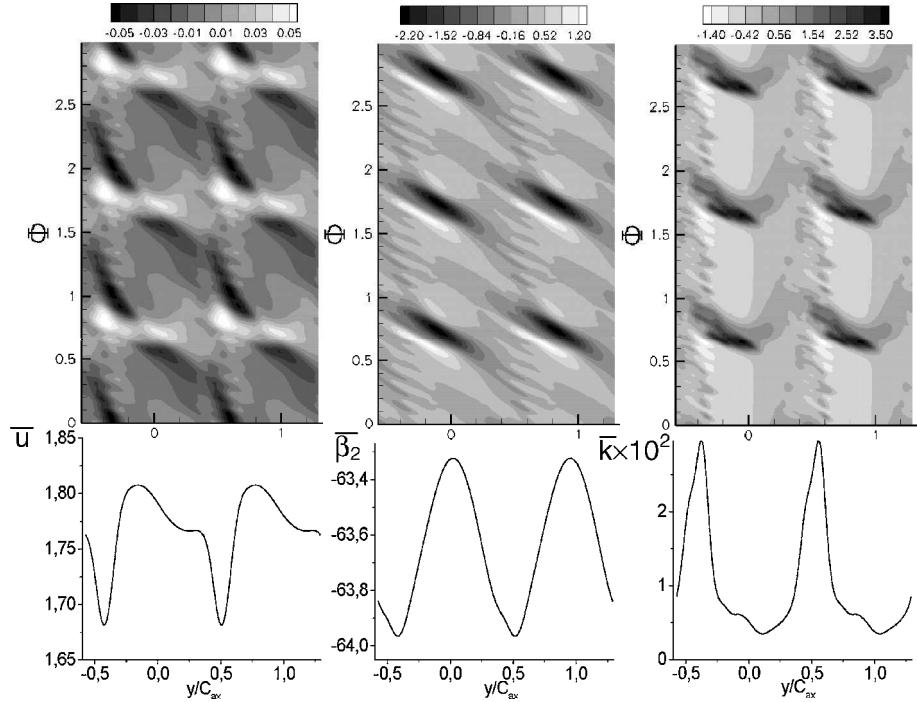

Fig. 23   Space–time plots of phase-averaged velocity magnitude, flow angle, and turbulent kinetic energy at $x/C_{ax} = 1.4$ (top row) and corresponding time-averaged quantities (bottom row).

VIII.   Flow Downstream of Trailing Edge

The flow downstream of the trailing edge is of importance because it gives a measure of the unsteadiness which survives from the incoming wakes and is transmitted to the next blade row. Because the interrow gap is generally in the range of 0.3–$0.5 \times C_{ax}$, Fig. 23 shows the velocity magnitude $\langle |U| \rangle$, the flow angle β_2, and the turbulent kinetic energy at a section located $0.4 \times C_{ax}$ downstream of the trailing edge. The lower plots show the time-averaged profiles along the pitch, whereas the space–time plots illustrate the fluctuations, triggered by the incoming wakes, of the phase-averaged quantities with respect to the time-averaged value. The time-averaged velocity magnitude has changes of approximately 10% of the mean in the pitchwise direction. Figure 23 also shows the positive–negative fluctuations in time due to the wakes; a positive–negative velocity defect (Fig. 5) is responsible for the local increase/decrease of $\langle |U| \rangle$. This fluctuation is of the order of $\pm 3\%$ of the local time-averaged velocity against the value of 18% imposed at the inlet. The average flow

angle is slightly larger than what was expected (63.6 deg against the design value of 63.2). The unsteadiness induced by the incoming wakes is at most 2 deg (Fig. 23, middle panel, top row). The plot of the turbulent kinetic energy reveals that the local phase-averaged fluctuations can be 10 times as large as the local time-averaged value. This large scatter is located on the suction side portion of the wake generated by the blade. In general, Fig. 23 reveals that the influence of the incoming wake is still visible $40\% C_{ax}$ downstream of the trailing edge. Although both flow velocity and angle are only slightly affected, the turbulent kinetic energy fluctuation peak is quite large. Thereby, the potential effect on the boundary layer of the next blade row is equally large.

IX.   Conclusions

The LES of the flow in a low-speed turbine cascade in the presence of incoming periodic wakes was first compared with an existing DNS. As expected, the flow structures captured by the LES

show less detail. Nevertheless, with 5.3 times fewer grid nodes, the present LES provided an overall picture and general flow pattern that agreed fairly well with that of the DNS,[8] as evidenced by the flow visualizations.

The analysis of the flow revealed that the complex mechanism that triggers the transition to turbulence of the suction-side boundary layer is not fully reproduced. LES predicts a transition point that is delayed by approximately 10% C_{ax} compared to DNS. The analysis of the results indicated that the resolution of the suction-side boundary layer is probably not sufficient to describe the fine-scale fluctuations and the turbulent spots. Moreover, some of the difficulties in reproducing the skin friction predicted by DNS may partly result from the SGS model and partly from the relatively (with respect to DNS) coarse grid in the flow core, which does not allow resolution of all of the fine-scale activity convected by the wake (Fig. 17). The phase-averaged plots showed interesting similarities with what was discovered during the experimental investigation of the flow in a similar low-speed turbine: the periodic appearance of turbulent and becalmed regions on the suction side of the blade was clearly triggered by the wake. A time delay between the onset of turbulence activity in the boundary layer and the position of the wake was also observed. Moreover, turbulence is shown to develop a fully three-dimensional state considerably after the first appearance of streamwise velocity fluctuations.

On the pressure side, there is much closer agreement with the DNS. This is probably due to the reduced effect of the impinging wakes and due to the largely laminar nature of the boundary layer. In fact, the analysis of the simulation revealed that the longitudinal vortices on the pressure side, the interaction with the wall of which promotes pairs of counter-rotating vortices, are potentially able to trigger transition. Nevertheless, due to the strong favorable pressure gradient, the strong streamwise velocity fluctuations associated with the longitudinal vortices never manage to promote sufficient levels of spanwise and normal stresses. Hence, the resolved turbulent stresses exhibit quite large anisotropy and the flow never develops fully three-dimensional turbulence.

The analysis of the exit flow shows that the effect of the incoming periodic wakes is quite evident, especially in the phase-averaged turbulent kinetic energy, which exhibits fluctuations that are one order of magnitude larger than the corresponding time-averaged value.

The results allow the conclusion that the flow pattern provided by the LES is, at least in the present case, sufficiently similar to that predicted by the DNS. In this view, LES can provide data for further RANS model development, with the exception of the transitional portion of the suction-side boundary layer, where better resolution is necessary. Overall, the computational effort is considerably reduced with respect to DNS. Therefore, LES can be expected to play an increasing role in solving flow problems of industrial relevance.

Acknowledgments

References

[1]Hummel, F., "Wake–Wake Interaction and its Potential for Clocking in a Transonic High-Pressure Turbine," *Journal of Turbomachinery*, Vol. 124, Jan. 2002, pp. 69–76.

[2]Michelassi, V., Martelli, F., Dénos, R., Arts, T., and Sieverding, C. H., "Unsteady Heat Transfer in Stator–Rotor Interaction by Two Equation Turbulence Model," *Journal of Turbomachinery*, Vol. 121, July 1999, pp. 436–447.

[3]Emunds, R., Jennions, I. K., Bohn, D., and Gier, J., "The Computation of Adjacent Blade-Row Effects in a 1.5-Stage Axial Flow Turbine," *Journal of Turbomachinery*, Vol. 121, 1999, pp. 1–10.

[4]Dénos, R., Arts, T., Paniagua, G., Michelassi, V., and Martelli, F., "Investigation of the Unsteady Rotor Aerodynamics in a Transonic Turbine Stage," *Journal of Turbomachinery*, Vol. 123, No. 1, 2001, pp. 81–89.

[5]Mayle, R. E., "The Role of Laminar-Turbulent Transition in Gas Turbine Engines," American Society of Mechanical Engineers, ASME Paper 91-GT-261, 1991.

[6]Cho, N.-H., Liu, X., Rodi, W., and Schönung, B., "Calculation of Wake-Induced Unsteady Flow in a Turbine Cascade," American Society of Mechanical Engineers, ASME Paper 92-GT-306, 1992.

[7]Wissink, J. G., "DNS of a Separating Low Reynolds Number Flow in a Turbine Cascade with Incoming Wakes," *Proceedings V International Symposium on Engineering Turbulence Modelling and Measurements*, Elsevier, Amsterdam, 2002, pp. 731–740.

[8]Wu, X., and Durbin, P. A., "Evidence of Longitudinal Vortices Evolved from Distorted Wakes in a Turbine Passage," *Journal of Fluid Mechanics*, Vol. 446, 2001, pp. 199–228.

[9]Mellen, C. P., Fröhlich, J., and Rodi, W., "Lessons from the European LESFOIL project on LES of Flow around an Airfoil," AIAA Paper 2002-0111, 2002.

[10]Moin, P., "Advances in Large Eddy Simulation Methodology for Complex Flows," 2nd TSFP, Vol. 1, 2001.

[11]Liu, X., and Rodi, W., "Experiments on Transitional Boundary Layers with Wake-Induced Unsteadiness," *Journal of Fluid Mechanics*, Vol. 231, 1991, pp. 229–256.

[12]Liu, X., and Rodi, W., "Velocity Measurements of Wake-Induced Unsteady Flow in a Linear Turbine Cascade," *Experiments in Fluids*, Vol. 17, 1994, pp. 45–48.

[13]Schulte, W., and Hodson, H. P., "Unsteady Wake-Induced Boundary Layer Transition in High Lift LP Turbines," *Journal of Turbomachinery*, Vol. 120, Jan. 1998, pp. 28–35.

[14]Stadtmüller, P., "Investigation of Wake-Induced Transition on the LP Turbine Cascade T106A-EIZ," German Research Foundation, DFG-Verbundprojekt Fo 136/11, Ver. 1.1, 2001.

[15]Stadtmüller, P., and Fottner, L., "A Test Case for the Numerical Investigation of Wake Passing Effects of a Highly Loaded LP Turbine Cascade Blade," American Society of Mechanical Engineers, ASME Paper 2001-GT-311, 2001.

[16]Michelassi, V., Wissink, J., and Rodi, W., "Analysis of DNS and LES of a Low-Pressure Turbine Blade with Incoming Wakes and Comparison with Experiments," Inst. for Hydromechanics, Rept. 789, Univ. of Karlsruhe, Karlsruhe, Germany, 2002; also *Flow, Turbulence and Combustion* (to be published).

[17]Wu, X., Jacobs, R. G., Hunt, J. C. R., and Durbin, P. A., "Simulation of Boundary Layer Transition Induced by Periodically Passing Wakes," *Journal of Fluid Mechanics*, Vol. 398, 1999, pp. 109–153.

[18]Huai, X., Joslin, R. D., and Piomelli, U., "Large Eddy Simulation of Transition to Turbulence in Boundary Layers," *Theoretical Computational Fluid Dynamics*, No. 9, 1997, pp. 149–163.

[19]Hsu, K., and Lee, L., "A Numerical Technique for Two-Dimensional Grid Generation with Grid Control at all of the Boundaries," *Journal of Computational Physics*, Vol. 96, 1991, pp. 451–469.

[20]Breuer, M., and Rodi, W., "Large Eddy Simulation for Complex Turbulent Flows of Practical Interest," *Flow Simulation with High Performance Computers II*, Notes on Numerical Fluid Mechanics, Vol. 52, Vieweg Verlag, 1996, pp. 258–274.

[21]Rhie, C. M., and Chow, W. L., "Numerical Study of the Turbulent Flow Past an Airfoil with Trailing-Edge Separation," *AIAA Journal*, Vol. 21, 1983, pp. 1525–1532.

[22]Germano, M., Piomelli, U., Moin, P., and Cabot, W. H., "A Dynamic Subgrid-Scale Eddy Viscosity Model," *Physics of Fluids A*, Vol. 3, No. 7, 1991, pp. 1760–1765.

[23]Lilly, D. K., "A Proposed Modification of the Germano Subgrid-Scale Closure Method," *Physics of Fluids A*, Vol. 4, No. 3, 1992, pp. 633–635.

[24]Jeong, J., and Hussain, F., "On the Identification of a Vortex," *Journal of Fluid Mechanics*, Vol. 285, 1995, pp. 69–94.

[25]Pope, S. B., *Turbulent Flows*, Cambridge Univ. Press, Cambridge, England, U.K., 2001.

[26]Rogers, M. M., "The Evolution of Strained Turbulent Plane Wakes," *Journal of Fluid Mechanics*, Vol. 463, 2002, pp. 53–120.

W. J. Devenport
Associate Editor